Appl. Phys. B 68, 833–842 (1999) / DOI 10.1007/s003409900026

Applied Physics B
Lasers
and Optics

Off-Bragg-angle light diffraction and structure of dynamic interband photorefractive gratings

P. Bernasconi, G. Montemezzani, P. Günter

Nonlinear Optics Laboratory, Institute of Quantum Electronics, Swiss Federal Institute of Technology, ETH Hönggerberg, CH-8093 Zürich, Switzerland
(Fax: +41-1/633-1056, E-mail: pbernasc@iqe.phys.ethz.ch)

Received: 23 November 1998/Revised version: 14 January 1999/Published online: 12 April 1999

Abstract. Steady-state and time-resolved off-Bragg-angle diffraction experiments are used to determine the structure and the dynamics of photorefractive gratings induced by interband photoexcitation. In potassium niobate, we identify in such gratings basically a two-layer structure. Close to the surface, we find a space-charge electric field generated by a charge modulation stored directly in the bands. This grating component is typically 50 μm thick, the amplitude of the refractive index modulation is larger than 10^{-4}, and the response time is a few μs for resonant intensities of 100 mW cm^{-2}. This component is also robust under non-resonant illumination. Deeper in the crystal, a second holographic layer extends over a few hundreds of μm, its amplitude is smaller, and its slower response time is in the ms range. The mutual phase shift between the grating components is also determined.

PACS: 42.40.Lx; 42.65.Hw; 77.84.Dy

Off-Bragg-angle light diffraction is an efficient tool to investigate the structure of holographic gratings for the determination of their best operation conditions. This technique consists of diffraction experiments in geometries where the Bragg condition, or momentum conservation, is not exactly fulfilled but, due to the finite spatial extent of the grating, a diffracted signal is still detectable [1]. In several works, the diffraction properties of off-Bragg conditions have been used successfully for example to evaluate the cross-talk noise, wavelength, and angular selectivity of multiplexed holographic gratings whose structure (amplitude, thickness, phase, ...) was known a priori [2–5]. In the present work, we show how time-resolved off-Bragg-angle diffraction can be very useful to investigate the strength profile as well as the dynamic response of holographic gratings. Due to their interesting and peculiar properties, our attention is focused on phase gratings created in electro-optic, photoconductive crystals by means of direct interband photoexcitation [6–9]. To our knowledge, this is the first systematic study of the temporal and the spatial holographic structure of interband photorefractive gratings in ferroelectric crystals.

Photorefractive gratings induced by direct band-to-band photoexcitations have shown several favorable properties. As compared with the conventional photorefractive gratings, they are faster, stronger, thinner, and very robust under non-resonant illumination [6–8, 10]. Experimentally, response times of a few μs with index changes larger than 10^{-4} have been already demonstrated even for intensities of few mWcm^{-2} in gratings with thickness of the order of 100 μm. These characteristics make the interband gratings well suited for example for high-resolution, high-speed, and low-power consumption applications for spatial light modulators or optical correlators [10], and for waveguide structures [9] or dynamic reconfigurable waveguide networks [11], as well as for material characterization [8, 12].

In a first theoretical part, we summarize the equations governing the photorefractive processes. To point out the peculiar characteristics of the interband effects, we compare the solutions for this case with the responses obtained in conventional approach. Based on the steady-state and the dynamics of the interband space-charge electric field and its intensity dependence, we propose a first model used to describe the space and time structure of interband photorefractive gratings. In the following experimental part, we present the holographic measurements performed in potassium niobate. According to our model we finally derive and discuss the main parameters required by the description of the interband photorefractive gratings.

1 Interband vs. conventional photorefraction

The photorefractive effect is a process in which a nonuniform spatial illumination induces an inhomogeneous charge distribution. The latter produces a space-charge electric field which, through the linear electro-optic effect, generates a modulation of the refractive indices of the medium. That is a phase grating. With *conventional* photorefraction we

We dedicate this article to Prof. Dr. Eckard Krätzig on the occasion of his 60th birthday. His contributions to the field of photorefraction have inspired and stimulated the scientific community over more than 20 years.

refer to the case where the charge migration is assisted by the absorption of photons with energy smaller than the material energy band gap [13] as schematically shown in Fig. 1a. There, the charge carriers are photoexcited into one of the bands from donors or acceptors levels lying in the band gap. After diffusion, drift, or photogalvanic effect they recombine into the acceptors or donors levels. *Interband* photorefraction, in contrast, relies on direct band-to-band charge photoexcitations induced by the absorption of photons whose energy exceeds the energy gap (Fig. 1b).

In both cases, the charge transport processes are described by a similar band-conduction model. Here, we consider a crystal with a single impurity level acting alternately as donor and acceptor. Under the assumption that the material is not dichroic [14], the charge distribution which leads to a space-charge electric field can be determined by the following system of equations:

$$\frac{\partial n}{\partial t} = gI + s_\mathrm{e} I(N_\mathrm{D} - N_\mathrm{D}^+) - \gamma_\mathrm{dir} n p - \gamma_\mathrm{e} n N_\mathrm{D}^+ + \frac{1}{e}\boldsymbol{\nabla} \boldsymbol{J}_\mathrm{e} \,, \tag{1a}$$

$$\frac{\partial p}{\partial t} = gI + s_\mathrm{h} I N_\mathrm{D}^+ - \gamma_\mathrm{dir} n p - \gamma_\mathrm{h} p (N_\mathrm{D} - N_\mathrm{D}^+) - \frac{1}{e}\boldsymbol{\nabla} \boldsymbol{J}_\mathrm{h} \,, \tag{1b}$$

$$\frac{\partial N_\mathrm{D}^+}{\partial t} = s_\mathrm{e} I(N_\mathrm{D} - N_\mathrm{D}^+) - \gamma_\mathrm{e} n N_\mathrm{D}^+ + \gamma_\mathrm{h} p (N_\mathrm{D} - N_\mathrm{D}^+) - s_\mathrm{h} I N_\mathrm{D}^+ \,, \tag{1c}$$

$$\boldsymbol{J}_\mathrm{e} = en \overleftrightarrow{\mu}_\mathrm{e} \boldsymbol{E} + k_\mathrm{B} T \overleftrightarrow{\mu}_\mathrm{e} \nabla n \,, \tag{1d}$$

$$\boldsymbol{J}_\mathrm{h} = ep \overleftrightarrow{\mu}_\mathrm{h} \boldsymbol{E} - k_\mathrm{B} T \overleftrightarrow{\mu}_\mathrm{h} \nabla p \,, \tag{1e}$$

$$\boldsymbol{\nabla}(\epsilon_0 \overleftrightarrow{\epsilon} \boldsymbol{E}) = e(N_\mathrm{D}^+ + p - n - N_\mathrm{A}) \,. \tag{1f}$$

Here, n and p are the free or quasi-free [7] electron and hole concentrations in the conduction and in the valence band, N_D and N_D^+ are the concentrations of donors and ionized donors, and N_A is the concentration of ionized donors in the dark. $\boldsymbol{J}_\mathrm{e}$ and $\boldsymbol{J}_\mathrm{h}$ are the electron and hole current density vectors, $\boldsymbol{E}$ is the total electric field in the crystal, and I is the light intensity. The band-to-band photoexcitation constant $g \equiv \alpha_\mathrm{dir}/h\nu$ is defined as the absorption constant α_dir in an impurity-free crystal divided by the corresponding photon energy $h\nu$, γ_dir is the band-to-band recombination constant. Similarly, we have the photoionisation constant s_e, s_h and the recombination constants γ_e, γ_h for electrons and holes, respectively, for transitions from and to the traps. The electron and the hole mobility tensors are denoted by $\overleftrightarrow{\mu}_\mathrm{e}$ and $\overleftrightarrow{\mu}_\mathrm{h}$, ϵ_0 is the vacuum permittivity and $\overleftrightarrow{\epsilon}$ the effective [15] dielectric permittivity tensor, e is the unit charge, k_B is the Boltzmann constant, and T is the absolute temperature. In this approach we neglect thermal charge excitation and we do not consider contributions to the charge transport due to photogalvanic currents.

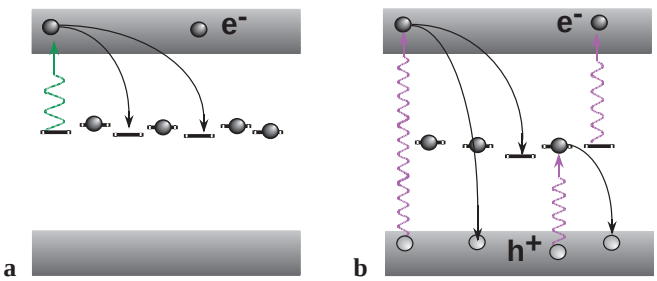

Fig. 1a,b. Schematic band-conduction models for conventional single-level, singlecharge carrier, photorefraction (**a**) and for interband photorefraction (**b**)

The conventional photorefractive space-charge electric field can determined from (1a)–(1f) by setting $g = \gamma_\mathrm{dir} = s_\mathrm{h} = \gamma_\mathrm{h} = 0$, which corresponds to the well-known single-level, single-charge-carrier species band-conduction model [13, 16]. For brevity we report here only the steady-state value of the photoconductivity $\sigma = en_0\mu_\mathrm{e}$ and the dynamics of the space-charge field E_sc. The spatial average of the electron density in the conduction band at steady-state under an illumination I_0 converges to

$$n_0 = \frac{s_\mathrm{e} I_0}{\gamma_\mathrm{e}} \left(\frac{N_\mathrm{D} - N_\mathrm{A}}{N_A} \right) \,, \tag{2}$$

while the space-charge field, after switching on a sinusoidal spatial light distribution with small modulation depth m and with grating wavevector $\boldsymbol{K}$, evolves as

$$E_\mathrm{sc} = -\mathrm{i}m \frac{E_\mathrm{q}(E_\mathrm{D} - \mathrm{i}E_0)}{E_\mathrm{q} + E_\mathrm{D} - \mathrm{i}E_0} \left(1 - e^{\Gamma t}\right) \,, \tag{3}$$

where the complex exponential time rate is

$$\Gamma = -\frac{\sigma}{\epsilon_\mathrm{eff}\epsilon_0} \times \frac{\left[E_\mathrm{R}(E_\mathrm{D} + E_\mathrm{R})(E_\mathrm{D} + E_\mathrm{q}) + E_0^2\right] + \mathrm{i}\left[E_0 E_\mathrm{R}(E_\mathrm{q} - E_\mathrm{R})\right]}{E_\mathrm{q}\left[(E_\mathrm{D} + E_\mathrm{R})^2 + E_0^2\right]} \,. \tag{4}$$

Besides the external electric field E_0, we have the diffusion, the trap-limited, and the recombination fields

$$E_\mathrm{D} \equiv \frac{k_\mathrm{B} T}{e} K \,, \quad E_\mathrm{q} \equiv \frac{e}{\epsilon_\mathrm{eff}\epsilon_0 K} N_\mathrm{eff} \,, \quad E_\mathrm{R} \equiv \frac{\gamma_\mathrm{e} N_\mathrm{A}}{\mu_\mathrm{e} K} \,, \tag{5}$$

where the effective trap density is given by

$$N_\mathrm{eff} \equiv \frac{N_A(N_\mathrm{D} - N_A)}{N_\mathrm{D}} \,. \tag{6}$$

The decay under homogeneous illumination follows a single exponential function with the same characteristic time rate Γ.

On the other hand, in the interband case the direct band-to-band transitions play the main role because of the strong resonant absorption. In fact, it has already been demonstrated theoretically and experimentally that optically induced interband effects can easily dominate over the impurity-to-band transitions [6–8, 10] so that for high enough intensities the crystal can be considered as trap-free. Equations (1a)–(1f) can be then simplified by setting $s_\mathrm{e} = s_\mathrm{h} = \gamma_\mathrm{e} = \gamma_\mathrm{h} = 0$. At steady-state the spatial average of the charge concentration in the bands is

$$n_0 = p_0 = \sqrt{gI_0/\gamma_\mathrm{dir}} \,. \tag{7}$$

In contrast to the conventional one-level, one-carrier model where the charge density grows linearly with the light intensity (see (2)), under interband illumination the growth is proportional to the square root as a direct consequence of the interband excitation and recombination processes. After switching on a modulated intensity we then obtain the evolution of the amplitude of the spatially modulated space-charge field

$$E_{\mathrm{sc}}(t) = -\mathrm{i}mA\left\{1-\frac{1}{2}\left[(1-B/C)e^{\Gamma_1 t}+(1+B/C)e^{\Gamma_2 t}\right]\right\}, \tag{8}$$

where

$$A \equiv \frac{E_{\mathrm{qf}}\left[E_{\mathrm{D}}(E_{\mathrm{Re}}-E_{\mathrm{Rh}})+\mathrm{i}E_0(E_{\mathrm{Re}}+E_{\mathrm{Rh}})\right]}{(E_{\mathrm{D}}+E_{\mathrm{Re}}+E_{\mathrm{Rh}})(E_{\mathrm{D}}+2E_{\mathrm{qf}})+\mathrm{i}E_0(E_{\mathrm{Re}}-E_{\mathrm{Rh}})+E_0^2}, \tag{9a}$$

$$B \equiv (E_{\mathrm{D}}+E_{\mathrm{qf}})(E_{\mathrm{Re}}+E_{\mathrm{Rh}})+\mathrm{i}E_0(E_{\mathrm{Re}}-E_{\mathrm{Rh}})+2E_{\mathrm{Re}}E_{\mathrm{Rh}}, \tag{9b}$$

$$C \equiv \left\{\left[(E_{\mathrm{D}}+E_{\mathrm{qf}})(E_{\mathrm{Re}}-E_{\mathrm{Rh}})-\mathrm{i}E_0(E_{\mathrm{Re}}+E_{\mathrm{Rh}})\right]^2 + 4E_{\mathrm{Re}}E_{\mathrm{Rh}}(E_{\mathrm{qf}}-E_{\mathrm{Re}})(E_{\mathrm{qf}}-E_{\mathrm{Rh}})\right\}^{1/2}. \tag{9c}$$

The exponential time rates $\Gamma_{1,2}$ are given by

$$\Gamma_{1,2} \equiv -\frac{\sqrt{\gamma_{\mathrm{dir}} g I_0}}{2E_{\mathrm{Re}}E_{\mathrm{Rh}}}(B \mp C). \tag{10}$$

In analogy, we define the free-carrier-limited, the electron and hole recombination fields as

$$E_{\mathrm{qf}} \equiv \frac{e}{\epsilon\epsilon_0 K}\sqrt{\frac{gI_0}{\gamma_{\mathrm{dir}}}}, \quad E_{\mathrm{Re/Rh}} \equiv \frac{1}{K\mu_{e/h}}\sqrt{\frac{gI_0}{\gamma_{\mathrm{dir}}}}. \tag{11}$$

With these definitions it can be shown that $\mathrm{Re}\{\Gamma_{1,2}\} < 0$. The evolution during the decay is given by the square bracket in (8).

Without going into details, we point out the main differences between the conventional and the interband space-charge field. Equation (8) demonstrates that a space-charge electric field can be produced by spatially modulating the free hole and the free electron density distributions alone, that is even in the absence of deep trapping sites. Such gratings are also robust under non-resonant illumination, i.e. they are practically not affected by light with wavelength longer than the fundamental absorption edge [7, 8, 10].

Further, it can be shown that when $E_{\mathrm{D}} \gg E_{\mathrm{D}}$ or $E_{\mathrm{D}} \gg E_{\mathrm{Re/Rh}}$ the amplitude of E_{sc} increases with the intensity in contrast to conventional photorefraction where E_{sc} is intensity independent and limited by N_{eff}. Depending on the relative efficiency of the photoexcitation and the recombination processes in (7), the intensity dependence may produce very large densities of free charges which lead to larger amplitudes of E_{sc}. Larger charge densities increase also the photoconductivity which contributes to the fast response of interband effects. A square-root decrease of the characteristic times for an increasing intensity is expected from (10).

Due to the large absorption the interband gratings cannot be used for two of the most popular applications of the photorefractive effect; coherent beam amplification, and phase conjugation [13]. Nevertheless, the absorption can be used to confine the photoexcitation processes over an extent of the order of the light penetration depth below the illuminated surface, so that thinner gratings can be recorded. An adjustment of the grating thickness can be achieved by tuning the illuminating wavelength inside the fundamental absorption band.

2 Grating profile

Compared with the well-behaved conventional gratings, interband holograms present new features in both temporal and spatial grating evolution. We propose here a first model used to illustrate the main characteristics of gratings induced by interband photoexcitation. As we shall elaborate below, our approach consists of a two-layer grating whose components have different amplitudes, thicknesses, response times, and phases as schematically shown in Fig. 2. Mathematically, the change of the refractive index Δn produced by switching on a spatial sinusoidal intensity modulation with grating wavevector $\boldsymbol{K}$ is described by

$$\Delta n(t, y) = \begin{cases} \Delta n_{\mathrm{b}}(1-e^{-t/\tau_{\mathrm{b}}})\cos(Kz) & 0 < y < d_{\mathrm{b}} \\ \Delta n_{\mathrm{t}}(1-e^{-t/\tau_{\mathrm{t}}})\cos(Kz+\Phi) & d_{\mathrm{b}} < y < d_{\mathrm{b}}+d_{\mathrm{t}}, \end{cases} \tag{12}$$

where d_{b} and d_{t} are the thicknesses of the two layers. The amplitudes are assumed to converge asymptotically to the steady-state values with the characteristics times $\tau_{\mathrm{b,t}}$. Φ is the mutual phase shift between the two grating components.

2.1 Interband photoconductivity

The typical intensity dependence of the interband photoconductivity [7, 8] is shown in Fig. 3. There, we recognize two distinct regimes: a linear and a square-root dependence for low and higher intensities, respectively. In the high-intensity

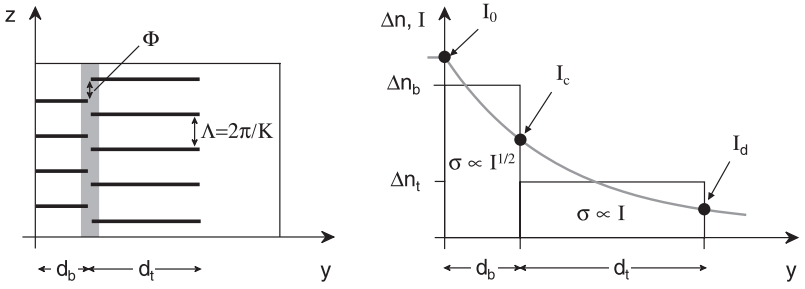

Fig. 2. Top view (*left*) and side view (*right*) of the model of the two-layer structure of the interband photorefractive gratings. Close to the surface, the space-charge modulation is due to free charges in the bands with refractive index change amplitude Δn_{b} and thickness d_{b}. The deeper component is due to charges in deep traps and has amplitude Δn_{t} and thickness d_{t}. The two grating components might be mutually phase shifted by Φ. The *gray curve* represents the light intensity: I_0 is the incident intensity, I_{c} is the critical intensity dividing the linear and the square-root intensity regime of the photoconductivity, I_{d} is the dark intensity

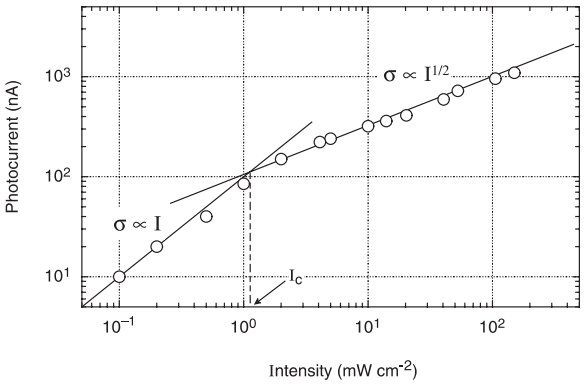

Fig. 3. Intensity dependence of the photocurrent under interband photoexcitation in nominally pure $KNbO_3$. Sample thickness: 47 μm, light wavelength: $\lambda = 364$ nm, electric field along the spontaneous polarization: $E = 250\,\mathrm{V\,cm^{-1}}$. The *full lines* represent the linear and the square-root intensity dependence, respectively

regime, the direct band-to-band transitions dominate over the transition channels involving the deep traps [7, 8]. The square-root dependence of the photoconductivity σ appears as in a trap-free crystal in agreement with (7). The influences of the trapping sites become evident only at lower intensities when the band-to-trap transitions dominate the charge recombination processes. Here, σ grows linearly with the intensity as can be shown by solving numerically [7, 9] the whole system of equations (1a)–(1f). We define the transition intensity I_c between the two regimes as shown in Fig. 3.

Note that a square-root dependence may occur also in case of quadratic recombination between the bands and the traps. However, this contribution can be safely neglected especially when the trap concentration is small as in the case of nominally pure crystals [7–9].

2.2 Charge modulation: bands vs. deep traps

The intensity dependence of σ suggests a variation of the strength of the photorefractive grating over the medium depth due to the strong resonant absorption. Close to the surface, i.e. in a high intensity regime, we expect E_{sc} to be described by (8), i.e. produced by a band charge-density modulation as in a trap-free crystal. In the following, we will refer to this grating component as the band grating. In fact for dominant interband transitions, the deep traps are practically completely filled or emptied so that no appreciable charge modulation is stored in such levels [7].

Deeper below the crystal surface, in the low-intensity regime, the charge modulation in the traps dominates so that a space-charge field with characteristics similar to the conventional photorefractive fields is expected. This is what we call the trap grating.

Because two kinds of gratings with rather distinct characteristics are involved, it is reasonable to model the interband grating morphology by the two-layer structure proposed above. The two grating components are spatially separated with distinct amplitudes, thicknesses, and response times. Of course, this sharp distinction is oversimplified, in reality the two parts smoothly fade one into the other. However, we will show below that even with this simplification, the experimental observations can be described in a very satisfactory way.

2.3 Amplitudes of the band and the trap gratings

As long as $E_D \gg E_{qf},\ E_{Re/Rh}$, the amplitude of the pure interband E_{sc} increases with the square root of the absorbed intensity as described by (8). Thanks to the efficient photoexcitation processes, E_{sc} can easily become stronger than in the traps.

In the deeper grating layer, E_{sc} undergoes the limitations imposed by N_{eff} similar to the conventional photorefraction (see (3)). We then expect the amplitude of the space-charge field to be roughly intensity independent. The amplitude profile of the charge modulation in this layer does not vary with the incident intensity as long as the incident intensity is higher than the dark intensity I_d, i.e. the intensity needed to produce a photoconductivity $\sigma = \sigma_d$.

The amplitude profile of both gratings is chosen to be of rectangular shape as shown by (12) and Fig. 2.

2.4 Thicknesses of the band and the trap gratings

The pure interband grating extends until the transition depth where the intensity is of the order of I_c. Since the intensity in the crystal decreases exponentially, according to our model we expect the transition point to move deeper in the sample logarithmically with the incident intensity I_0

$$d_b = \frac{1}{\alpha}\ln(I_0/I_c)\ . \tag{13}$$

Beyond this point, the charge modulation in the traps dominates and penetrates into the crystal as long as the photoconductivity stays larger than the dark conductivity σ_d of the material:

$$d_t = \frac{1}{\alpha}\ln(I_0/I_d) - d_b = \frac{1}{\alpha}\ln(I_c/I_d)\ . \tag{14}$$

In fact, beyond d_t thermal excitation from the traps, which we neglect in our model, prevents any charge modulation being generated.

Like its amplitude, also the thickness of the trap grating does not depend on the illuminating intensity provided that $I_0 > I_c$. The only influence of the intensity is to approach the trap grating close to the surface or to push it deeper inside the crystal.

2.5 Response times of the band and the trap gratings

Below the crystal surface, we expect a fast grating response of the order of the photoconductivity rise time, i.e. in the μs time scale [7, 8]. This time constant is expected to be inversely proportional to the square root of the intensity as predicted by (10).

Deeper in the crystal, the temporal evolution of the phase grating should be slower due to the reduced intensity and due to the strong influences of the transition involving the traps. The response time of the trap grating should be in the ms range as in conventional photorefractive experiments.

The dynamics of the grating amplitudes is simulated in (12) through a single time constant which describes the exponential responses of each component. Actually, for the band grating (8) demonstrates that the temporal evolution consists

of more elaborated behavior which, for the sake of simplicity, is empirically approximated by a single exponential function. Because of the intensity dependence of the response times, τ_b and τ_t have to be interpreted as average time constants of each grating layer. The thicknesses have been assumed to be time independent.

2.6 Phase shift between the band and the trap gratings

The sign of the majority charge carrier assumes a fundamental importance for the determination of the phase shift between the space-charge field and the intensity light pattern [13]. Since it cannot be excluded that the sign of the majority charge carriers changes with the intensity, the possibility that the two grating components are mutually phase shifted has to be taken into account.

In the case of pure diffusive charge transport, the mutual phase shift between the modulated electric fields in the two layers is either 0 or π. The effect of such a phase shift is extremely important for the diffraction strength of the interband grating. If the two components are in phase, under the exact Bragg angle the light diffracted by the two layers interferes constructively, whereas if the phase shift is π the interference is destructive, reducing the diffraction efficiency of the system.

3 Off-Bragg-angle diffraction experiments

The experiments are performed in samples of nominally pure, single-domain potassium niobate ($KNbO_3$) crystals. This material has been chosen because of its excellent photorefractive properties in the interband regime [7–10]. $KNbO_3$ is a ferroelectric material with perovskite structure. At room temperature, its phase structure is orthorhombic (point group mm2) with the crystallographic *b* axis in the pseudo-cubic [010] direction, while the *a* and *c* axes lie along the pseudo-cubic [101] and [$\bar{1}$01] directions. The spontaneous polarization P_S is oriented along the *c* axis and the energy band-gap amounts to $E_{gap} \approx 3.3$ eV at room temperature [17].

The investigation of the interband photorefractive gratings is performed through Bragg diffraction experiments in a conventional non-degenerate four-wave-mixing configuration as shown in Fig. 4. The holographic grating is recorded by two interfering ultraviolet *s*-polarized laser beams at $\lambda = 364$ nm ($h\nu = 3.4$ eV) while the read-out process is performed by the diffraction of a third probe beam at $\lambda = 633$ nm. The *p*-polarized read-out beam has a photon energy ($h\nu = 2.0$ eV) smaller than the energy gap in order to avoid influences on the band-to-band processes. The relevant optical absorption at the ultraviolet wavelength [7, 17] is $\alpha_a \approx \alpha_c = 540\ \mathrm{cm}^{-1}$ whereas in the visible it is $\alpha = 0.1\ \mathrm{cm}^{-1}$.

The strength of the space-charge electric field is determined by measuring the intensity of the diffracted probe signal [18]. The light diffracted by this layered structure is interpreted as the coherent sum of the waves diffracted by each grating component [18, 19] as shown in Fig. 4.

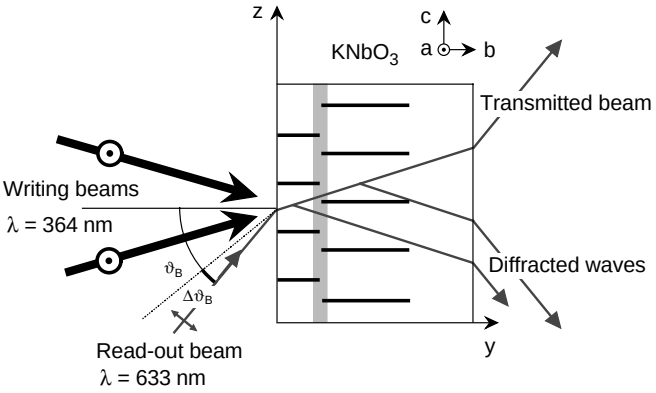

Fig. 4. Schematic set-up of a non-degenerate four-wave-mixing configuration. Two interfering beams record the interband grating while a third non-resonant beam incident close to the Bragg angle ϑ_B is diffracted at the two layers of the hologram

According to (12) and noting that $\epsilon = n^2$, during the grating build-up, the amplitude of the output scattered wave is

$$\begin{aligned} E(t, \boldsymbol{k}_d) &\propto \int \Delta\epsilon(t, \boldsymbol{r}) e^{i\boldsymbol{q}\boldsymbol{r}} \mathrm{d}\boldsymbol{r} \\ &\propto \delta(q_x)\delta(K - q_z) \\ &\quad \times \Bigg[\Delta\epsilon_b (1 - e^{-t/\tau_b}) \frac{\sin(q_y d_b/2)}{q_y} e^{iq_y d_b/2} \\ &\quad + \Delta\epsilon_t (1 - e^{-t/\tau_t}) \frac{\sin(q_y d_t/2)}{q_y} e^{iq_y d_t/2} \\ &\quad e^{i(q_y d_b - \Phi)} \Bigg], \end{aligned} \tag{15}$$

where $\boldsymbol{k}_d$ and $\boldsymbol{k}_i$ are the wavevectors of the diffracted and the incident read-out wave, and $\boldsymbol{q} \equiv \boldsymbol{k}_d - \boldsymbol{k}_i$ is the momentum mismatching. Thus the diffracted intensity is $I_d(\boldsymbol{k}_d) \propto E(\boldsymbol{k}_d) E^*(\boldsymbol{k}_d)$.

3.1 Steady-state experiments

From the angular selectivity of the Bragg condition, the thickness and the amplitude of the diffraction grating can be determined [18]. The following experiments are performed in 2-mm- and 47-μm-thick pure samples at a grating period of 0.5 μm by scanning the incident angle of the probe beam around the calculated exact Bragg angle. In order to observe the interband effects, the total ultraviolet intensity is kept constant to a value of $150\ \mathrm{mW\,cm}^{-2}$, well above the threshold intensity I_c.

In the 47-μm-thick samples an unusual double-peaked angular selectivity of the Bragg condition appears as can be clearly seen in Fig. 5. The maximum of the diffraction efficiency is measured for an incident angle different from the exact Bragg angle. The curve is qualitatively equivalent for grating periods up to 5 μm and also independent of the diffraction configuration (isotropic or anisotropic [13]). Because of the small diffraction efficiency and the reduced grating thickness, this peculiar shape can be only explained by a diffraction grating consisting of at least two *distinct* components placed at two *distinct* regions in the crystal. The symmetry of the curve

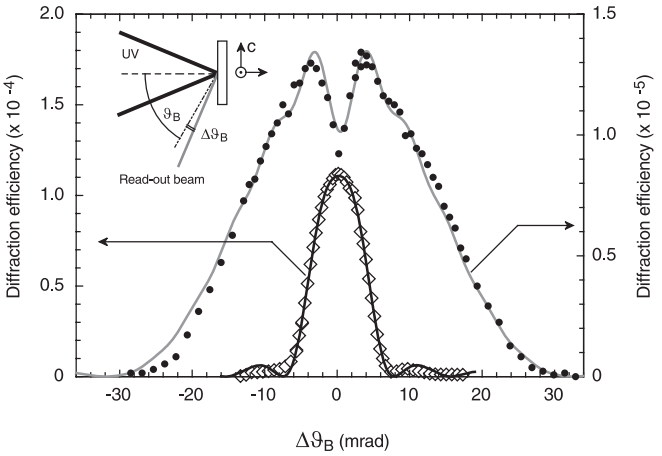

Fig. 5. Measured angular selectivity of the diffraction efficiency for isotropic Bragg diffraction in a 47-μm-thin (●) and in a 2-mm-thick (◇) sample. In both samples $\Lambda_g = 0.5\,\mu m$ along the c axis. The total writing intensity at $\lambda = 364\,nm$ is $150\,mW\,cm^{-2}$ with a modulation depth $m = 0.2$. The *full lines* are curves calculated according to (15)

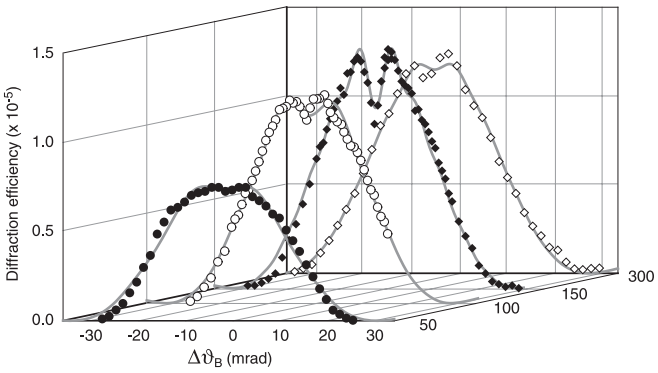

Fig. 6. Measured angular selectivity of the diffraction efficiency for isotropic Bragg diffraction in a 47-μm-thin sample for different ultraviolet writing intensities at $\lambda = 364\,nm$. $\Lambda_g = 0.5\,\mu m$ along the c axis and the modulation depth $m = 0.2$. The *full lines* are curves calculated according to (15)

indicates also that the two grating components must be mutually phase shifted by $\approx \pi$. This implies that at a certain depth, and thus at a given intensity, the majority charge carriers change the sign. With this kind of diffraction experiment, however, it is not possible to identify the absolute value of the majority carriers. An answer will be given below by two-wave-mixing experiments.

In the thick samples (Fig. 5), the evidence about the grating structure is masked because in this case the diffraction process is dominated by the trap grating. The half width at half maximum (HWHM) of the sharper angular selectivity indicates a grating thickness $d_{tot} \approx \lambda/\mathrm{HWHM} \approx 160$–$180\,\mu m$. Therefore, it can be concluded that in the thin sample the trap grating is always limited by the crystal size. So, if in the thin sample the diffraction strengths of the two grating components are comparable, in the thick sample the deeper layer dominates and prevents resolving of the two components. This is also supported by the stronger diffraction efficiency measured in the thick sample. The disappearing of the double-peak curve might also be attributed to a zero phase shift between the grating components. However, the dynamics of the diffraction efficiency will demonstrate that this is not the case in these experiments.

3.1.1 Intensity dependence. The angular selectivity of the Bragg condition is also sensitive to the intensity as shown in Fig. 6. By varying the total writing intensity from 50 to $300\,mW\,cm^{-2}$ in the 47-μm-thick samples, we increase amplitude and thickness of the band grating (see (8) and (13)) and the trap component is squeezed to the back of the crystal.

This becomes evident when looking at the parameters d_b, d_t, and $(\Delta\epsilon_b/\Delta\epsilon_t)$ obtained by fitting the measurements according to (15) at steady-state ($t \to \infty$). In fact, the results obtained in thin and thick samples are reported in Table 1. The change of relative strength and thicknesses influences the degree of competition between the π-shifted components and modifies the angular selectivity of the Bragg condition.

The thicknesses of the two grating components listed in Table 1 are in good agreement with the values estimated from simple photoconductivity arguments. In our samples

Table 1. Intensity dependence of the thickness at steady state of the band and the trap grating components and the relative amplitude obtained in a 47-μm-thin and in a thick sample. The values are obtained by fitting the curves shown in Figs. 5 and 6 according to (15)

$I_{UV}\,(mW\,cm^{-2})$	$d_b\,(\mu m)$	$d_t\,(\mu m)$	$\Delta n_b\,(\Delta n_t)$
Thin crystal			
50	13 ± 1	34 ∓ 1	4.2 ± 0.8
100	15 ± 1	32 ∓ 1	6.3 ± 0.8
150	18 ± 1	29 ∓ 1	7.1 ± 0.8
280	21 ± 2	26 ∓ 2	9.0 ± 0.8
Thick crystal			
100	16 ± 3	170 ± 30	6.7 ± 1.1
150	20 ± 3	190 ± 30	7.4 ± 1.1

$I_c = 1 - 10\,mW\,cm^{-2}$ so that for an incident intensity of $150\,mW\,cm^{-2}$, according to (13) the pure interband grating should extend over $d_b \approx 50\,\mu m$ below the surface. Further, in pure $KNbO_3$ the typical value of the dark conductivity [20] is of the order of $10^{-12}\,\Omega^{-1}\,cm^{-1}$ which corresponds to $I_d \approx 0.05\,mW\,cm^{-2}$. These values, according to (14), yield an estimated thickness of the deeper layer of $d_t \approx 150$–$200\,\mu m$.

As shown in Fig. 7, the thickness of the band grating appreciably increases with the incident intensity, in satisfactory agreement with the logarithmic behavior predicted by (13). On the other hand, the thickness of the trap grating stays constant when it is not limited by the crystal size, in agreement with (14).

The square-root dependence of the amplitude of the band grating component is also found in good agreement with the experimental results shown in Fig. 7. By comparing theory and experiments, we assumed the amplitude of the trap grating component to be primarily intensity independent as experimentally confirmed by Bragg diffraction measurements performed in the transverse geometry[7].

No influence is noticed due to the intensity of the read-out laser beam when the intensity is increased up to $2.5\,W\,cm^{-2}$. This confirms a remarkable robustness of the ultraviolet induced grating with respect to illumination at this wavelength [7].

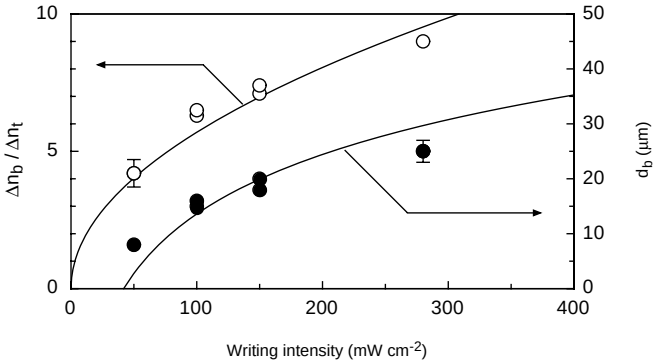

Fig. 7. Intensity dependence of the relative amplitude $\Delta n_b/\Delta n_t$ of the band and the trap grating components (○) in a thin sample fitted with a square-root function. In the same plot the intensity dependence of the thickness of the fast grating component (●) is compared with a theoretical logarithmic dependence

3.2 Time-resolved experiments

The diffraction experiments are performed in the thin samples with the identical configurations as before. The two writing beams are switched on and off by an acousto-optic deflector with 1 μs response time. The total ultraviolet intensity is chosen to be 150 mW cm^{-2} in order to observe the strongest competition between the two grating components.

3.2.1 Angular dependence. In all crystals, we recognize the presence of at least two distinct response times: A fast one in the μs time scale and a slower one in the ms region. The two regimes are associated with the rise and to a more or less pronounced relaxation of the diffraction efficiency. This kind of dynamics is typical of competing effects such as electron–hole competition [21–23] or electron–ion compensation [24–27]. However, these processes would lead to a scaling invariance of the diffraction efficiency as a function of the angular mismatching. This is clearly contradicted by the measurements as shown in Fig. 8. The lack of scaling invariance is therefore an additional indication that the grating consists of at least two distinct entities separated in space so that the effects mentioned above can be excluded.

According to our model, the angular dependence of the signal dynamics is explained by simple geometric reasons imposed by the grating structure. A variation of the incident angle of the read-out beam introduces a phase shift between the two waves diffracted at each grating layer as illustrated in Fig. 4 so that their overlapping leads to a more or less pronounced degree of constructive interference.

The measured dynamics of Fig. 8 is fitted according to (15) with the same parameter set consisting of thickness, amplitude, and response time of each grating component. Only the incident angle is varied. For the band grating here we obtained $d_b = 16 \pm 1\,\mu$m whereas the trap grating extends over the remaining $d_t = 31 \mp 1\,\mu$m. The relative amplitude $\Delta n_b/\Delta n_t$ is found to be 6.2 ± 1.1 in agreement with the results obtained at steady state and reported in Table 1. For all angular mismatchings, we obtained almost the same characteristic times. For this writing intensity of 150 mW cm^{-2}, the fast component associated with the band grating is $37 \pm 3\,\mu$s and the slow response time of the trap grating is found to be $320 \pm 40\,\mu$s.

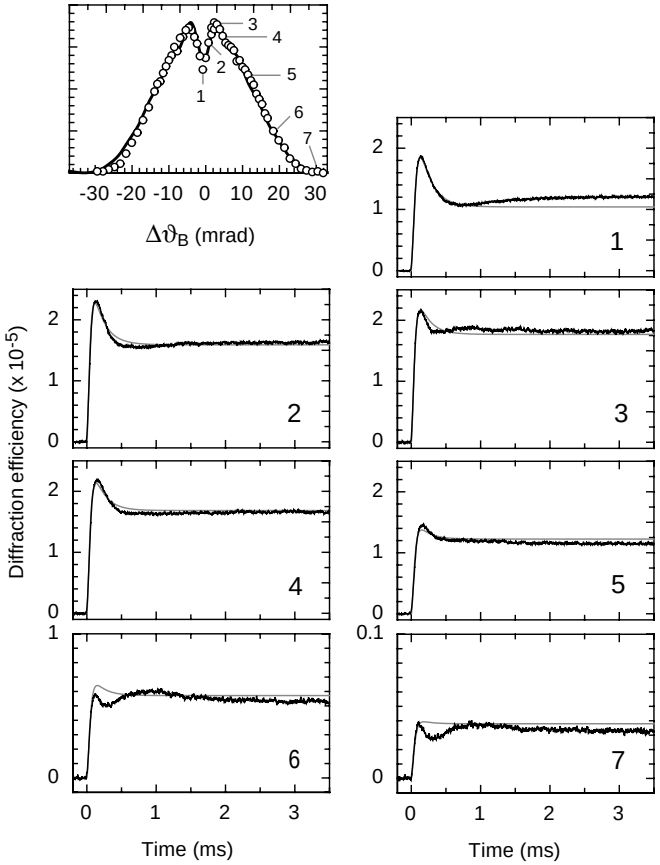

Fig. 8. Dynamics of the build-up of the diffraction efficiency for isotropic Bragg diffraction in a thin sample by varying the angle of incidence from position 1 to 7. $\Lambda_g = 0.5\,\mu$m along the *c* axis, and the total writing intensity is 150 mW cm^{-2} with a modulation depth $m = 0.2$. The *gray lines* are calculated according to (15)

The response times, the relative amplitudes, and the thicknesses of the grating components obtained from the fitting procedure described above have been used to simulate the dynamics of the angular rocking curve for Bragg diffraction. In Fig. 9 we see that shortly after the start of the process, the angular selectivity of the Bragg condition grows as a $\mathrm{sinc}^2(x)$ function typical of a single homogeneous diffraction grating that grows in amplitude. The response of the band grating is followed by the appearance of the trap grating which manifests itself by the deformation of the $\mathrm{sinc}^2(x)$ function to the double-peaked curve at the steady-state. In spite of the simplified model, the numerical simulations agree surprisingly well with the measured curves of Fig. 8.

3.2.2 Ultraviolet intensity dependence. The intensity dependence of the response times of each grating component is measured in a thin sample for a fixed incident angle of the read-out beam very close to the exact Bragg angle ($\Delta\vartheta <$ 2 mrad). As can be seen in Fig. 10, the dynamics of the diffracted signal clearly shows an enhancement of the compensation effects between the two gratings with decreasing intensity.

For an intensity of 0.6 mW cm^{-2} the diffracted signal disappears at steady state indicating that the diffraction strengths of the two grating components exactly balance each other. Below such intensity, the slow grating becomes stronger than

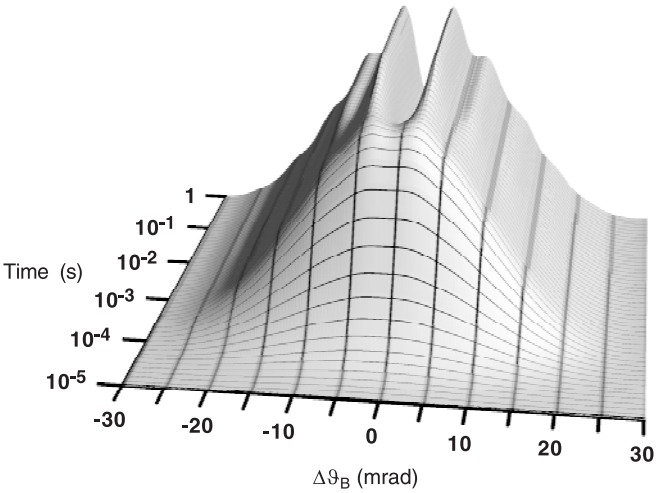

Fig. 9. Simulated time evolution of the angular selectivity of the Bragg condition in a 47-μm-thin sample. The grating parameters correspond to the values reported in Table 1 obtained by fitting the measured data for a total writing intensity of 150 mWcm^{-2}

its antagonist. The diffracted signal goes through a zero-crossing point before rising again due to the dominant trap grating. This compensation effect is shown even better during the dark decay of the signal where the fast decay of one grating reveals the presence of the other one through a sudden increase of the diffracted signal.

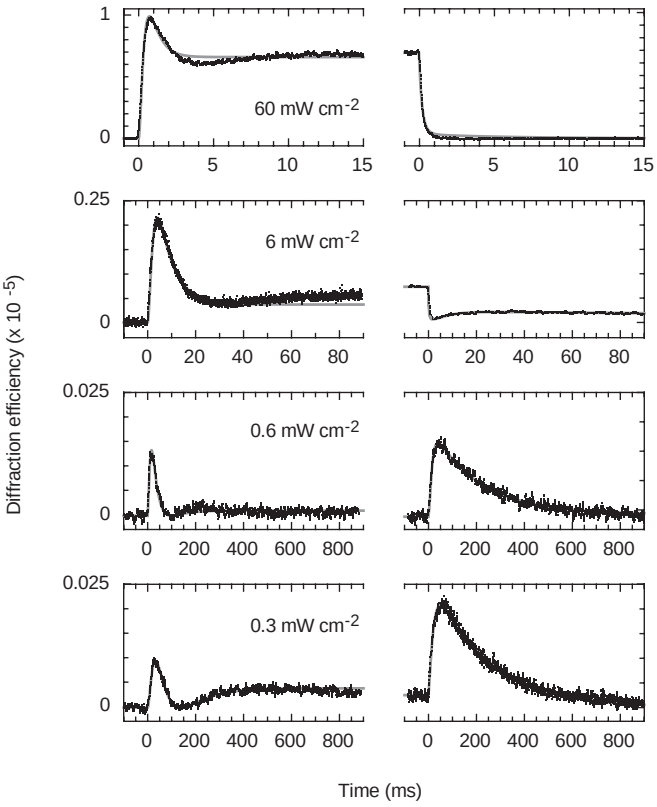

Fig. 10. Intensity dependence of the dynamics of the diffraction efficiency during the build-up (*left*) and the dark decay (*right*) for isotropic Bragg diffraction in a thin sample for a fixed angle of incidence very close to the exact Bragg angle ($\Delta\vartheta < 2$ mrad). The *gray lines* are calculated according to (15)

In Fig. 10, the dynamics of the diffracted signal is fitted according to (15). The thicknesses of the layers and the incident angle (q_y) are fixed. Note that for each incident intensity, both build-up and dark decay are fitted together with the same amplitudes and thicknesses but independent time constants.

The intensity dependence of the fast response time determined during the signal build-up is plotted in Fig. 11. In the intensity region where the quadratic recombination processes dominate, the response time decreases with the square root of the intensity as theoretically predicted by (10). The deviations of the data points from the square-root dependence for lower intensities are to be attributed to the influence of the traps which tend to slow down the build-up of the space-charge field.

The fast-time component of the dark decay is of the same order of the corresponding one determined during the signal build-up. On the other hand, the slow component of the dark decay is at least two orders of magnitude slower than the slow build-up response time. This is explained by considering that the dark decay of the trap grating relies on the conductivity generated by thermal charge excitation from the deep traps.

3.2.3 Influence of non-resonant illumination. It is known that a non-resonant illumination has virtually no influence on the pure interband photorefractive effect [7, 8, 10]. In contrast, the diffraction strength of the trap grating is expected to be reduced by the presence of an additional non-resonant illumination. The experiment is performed in the same configuration as before. The ultraviolet intensity is 1 mW cm^{-2} for which at steady state the compensation between the two competing gratings is almost complete. The homogeneous visible illumination at $\lambda = 514$ nm is ≈ 15 W cm^{-2}.

The dynamics of the diffracted intensity with and without the additional visible illumination can be compared in Fig. 12. The curves clearly show that the illumination in the visible increases the diffraction efficiency by drastically reducing the compensation effects. This result confirms that the trapping sites participate actively in the interband photorefractive process and are associated with the slow trap component. We

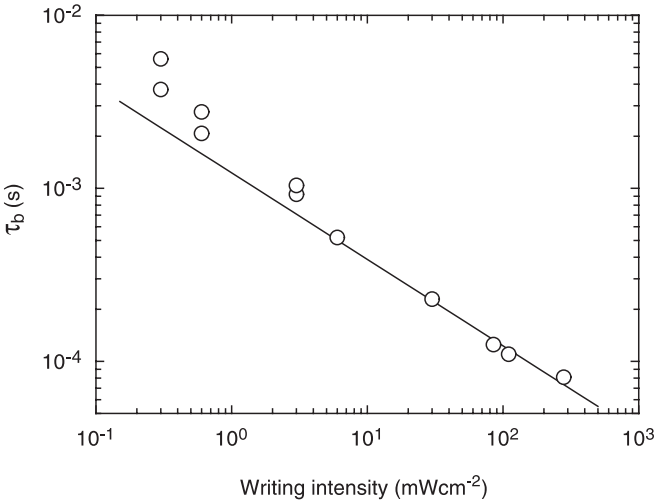

Fig. 11. Intensity dependence of response time of the fast grating component (○) in a thin sample compared to a theoretical power law dependence $I^{-\beta}$ ($\beta = 0.5$)

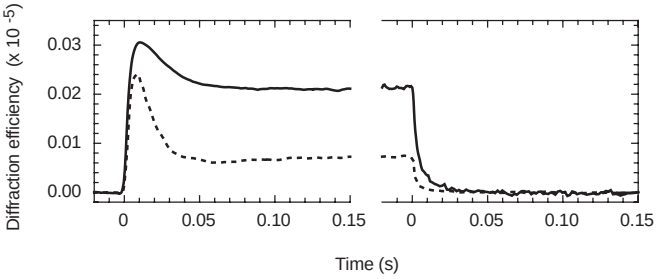

Fig. 12. Build-up and dark decay of the diffraction efficiency for isotropic Bragg diffraction in a thin sample for a fixed angle of incidence very close to the exact Bragg angle. The *full line* shows the diffraction efficiency when an additional homogeneous illumination of $\approx 15\,\mathrm{W\,cm^{-2}}$ at $\lambda = 514\,\mathrm{nm}$ is superimposed to the ultraviolet writing intensity of $0.6\,\mathrm{mW\,cm^{-2}}$. The *dotted line* shows the dynamics without any additional light

also observe that the response times are not appreciably modified by the presence of an additional visible illumination.

3.3 Relative phase shift between the band and the trap gratings

We have already pointed out that the interband grating components may be mutually phase shifted. In support of this statement we have three experimental evidences: the angular dependence of the Bragg selectivity, the compensation effects seen during the dynamics, and the intensity dependence of the sign of the coupling constant in two-wave-mixing experiments, which we are going to discuss now. All these three effects together cannot be explained without assuming a phase shift.

The two-wave-mixing experiments [13] have been performed in the same geometry shown in Fig. 4 by simply removing the probe beam. As shown in Fig. 13, where the two-wave-mixing exponential gain is plotted as a function of the intensity, around $I_c \approx 1\,\mathrm{mW\,cm^{-2}}$ the coupling constant changes sign. This means that the direction of the energy transfer between signal and pump is reversed. The energy transfer direction in the two-wave-mixing process depends on the phase between the refractive index modulation and the illuminating pattern [13]. In our case the charge transport is purely diffusive and the above change of sign of the coupling constant implies a jump in phase by π.

From the direction of the spontaneous polarization of the sample, the position of the two beams, and the sign of the coupling constant we find that for high intensities in this pure sample the interband photoconductivity is dominated by holes, in agreement with all previous measurements [7]. Therefore we conclude that for low intensities where the grating in the traps dominates the coupling process, the electrons are the majority carriers.

Note that for the measurements in Fig. 13, within the experimental accuracy, the same absolute values are obtained by exchanging the role of signal and pump. This proves that for writing intensities as high as $1\,\mathrm{W\,cm^{-2}}$, the presence of absorption gratings can be neglected. Furthermore, diffraction experiments performed in a non-electro-optic configuration gave no detectable signal, confirming the latter conclusion.

We would like to remark that besides the case of a π phase-shift described above, we have also observed gratings

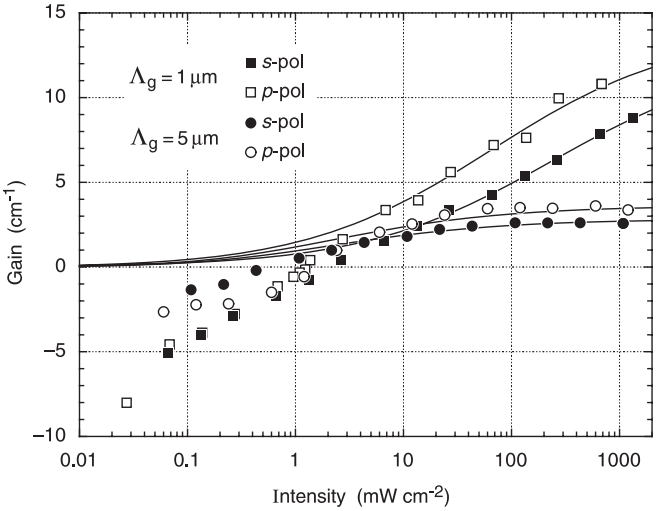

Fig. 13. Intensity dependence of the coupling gain for grating periods $\Lambda_g = 1\,\mu\mathrm{m}$ and $5\,\mu\mathrm{m}$ with *s*- and *p*-polarized light beams in a thin sample. The wavelength is $\lambda = 364\,\mathrm{nm}$ with a modulation depth $m = 0.11$. The *curves* are calculated according to (8) describing a trap-free crystal

whose two components are in phase, for example in iron-doped, ion-implanted $KNbO_3$ waveguides [28]. This means that in this crystal the photoconductivity results are dominated by the same charge carrier type for all intensity regimes.

4 Conclusions

Time-resolved off-Bragg-angle light diffraction experiments have been used to characterize interband photorefractive gratings in crystals of $KNbO_3$. The steady-state values and the dynamics of the diffraction efficiency allowed us to unambiguously identify a double-layered structure of the gratings. The two layers are related to the two distinct intensity regimes occurring under resonant illumination. We showed with the help of an interband-conduction model that for high intensities, the charge transitions which lead to the space-charge field are dominated by the direct band-to-band photoexcitation and recombination processes, whereas for low intensities the band-to-trap transitions play a major role. Therefore, close to the surface, the high-intensity light pattern records a phase grating through a band charge modulation, while deeper in the sample a phase grating is stored in deep traps. Amplitude, thickness, and response time of the grating components are found in very good agreement with the theoretical model.

Acknowledgements. We are very grateful to H. Wüest and to J. Hajfler for excellent sample preparation. This work has been supported by the Swiss National Science Foundation.

References

1. H. Kogelnik: Bell System Tech. J. **48**, 2909 (1969)
2. H. Zhou, F. Zhao, F.T.S. Yu: Appl. Opt. **33**, 4339 (1994)
3. R. Hofmeister, A. Yariv, S. Yagi: J. Opt. Soc. Am. A **11**, 1342 (1994)
4. S. Tau, Z.H. Song, D.R. Selviah: Opt. Commun. **108**, 144 (1994)
5. R. De Vré, M. Jeganathan, J.P. Wilde, L. Hesselink: Opt. Lett. **19**, 910 (1994)

6. G. Montemezzani, P. Rogin, M. Zgonik, P. Günter: Opt. Lett. **18**, 1144 (1993)
7. G. Montemezzani, P. Rogin, M. Zgonik, P. Günter: Phys. Rev. B **49**, 2484 (1994)
8. P. Bernasconi, G. Montemezzani, I. Biaggio, P. Günter: Phys. Rev. B **56**, 12196 (1997)
9. P. Bernasconi: PhD Thesis Nr.12761, ETH Zürich (1998)
10. P. Bernasconi, G. Montemezzani, M. Wintermantel, I. Biaggio, P. Günter: Opt. Lett. **24**, 199 (1999)
11. P. Dittrich, G. Montemezzani, P. Bernasconi, P. Günter: submitted to Opt. Lett.
12. P. Bernasconi, I. Biaggio, M. Zgonik, P. Günter: Phys. Rev. Lett. **78**, 106 (1997)
13. P. Günter, J.P. Huignard: *Photorefractive Materials and Their Applications I: Fundamental Phenomena* (Springer, Berlin, Heidelberg 1988)
14. G. Montemezzani, C. Medrano, P. Günter, M. Zgonik: Phys. Rev. Lett. **79**, 3403 (1997)
15. M. Zgonik, R. Schlesser, I. Biaggio, E. Voit, J. Tscherry, P. Günter: J. Appl. Phys. **74**, 1287 (1993)
16. N.V. Kuhktarev, V.B. Markov, S.G. Odulov, M.S. Soskin, V.L. Visnetskii: Ferroelectrics **22**, 961 (1979); N.V. Kuhktarev, V.B. Markov, S.G. Odulov, M.S. Soskin, V.L. Visnetskii: Ferroelectrics **22**, 949 (1979)
17. E. Wiesendanger: Ferroelectrics **6**, 263, (1974)
18. G. Montemezzani, M. Zgonik: Phys. Rev. E **35**, 1035 (1997)
19. R. De Vré, L. Hesselink: J. Opt. Soc. Am. B **13**, 285 (1996)
20. M. Ewart: PhD Thesis Nr.12484, ETH Zürich (1998)
21. F.P. Strohkendl, J.M. Jonathan, R.W. Hellwarth: Opt. Lett. **11**, 312 (1986)
22. G. Valley: J. Appl. Phys. **59**, 3363 (1986)
23. M.C. Bashaw, T.P. Ma, R.C. Barker, S. Mroczkowski, R.R. Dube: J. Opt. Soc. Am. B **17**, 2329 (1990)
24. G. Montemezzani, P. Günter: J. Opt. Soc. Am. B **7**, 2323 (1990)
25. G. Montemezzani, M. Zgonik, P. Günter: J. Opt. Soc. Am. B **10**, 171 (1993)
26. M.C. Bashaw, J.F. Heanue: J. Opt. Soc. Am. B **14**, 2024 (1997)
27. A. Yariv, S. Orlov, G. Rakuljic, V. Leyva: Opt. Lett. **20**, 1334 (1995)
28. D. Fluck, P. Günter, R. Irmscher, C. Buchal: Appl. Phys. Lett. **59**, 3213 (1991)